

Wind Resource Assessment and Numerical Simulation for Wind Turbine Airfoils

David Wafula Wekesa^{*‡}, Cong Wang^{*}, Yingjie Wei^{*} and Joseph N. Kamau[‡]

^{*}Institute of Dynamics and Control of Spacecrafts, School of Astronautics,
Harbin Institute of Technology, Heilongjiang, Harbin City 150001, P.R. China

[‡]Department of Physics, Jomo Kenyatta University of Agriculture & Technology, Nairobi City 00200, Kenya

Abstract—This paper investigates a feasibility measurement study for wind resource and a numerical simulation for wind regimes of Marsabit and Garissa stations, both rural-urban towns in Eastern region of Kenya. The experimental wind speed measurement was done using optical anemometer sensors while the wind direction was detected by wind vane sensors. The data logging instrumentation with calibrated wind sensors recorded higher resolution wind data. Based on the wind regimes at the sites, an analysis of aerodynamic performance and flow physics of two-dimensional numerical simulations on a NACA0015 airfoil was done using CFD FLUENT software. The Meteorological wind speed measurement correlated with the calibrated cup anemometer sensors measurement with a correlation coefficient of 0.98. The strong correlation confirms that the experimental anemometer gave the correct readings and practical readings can be approximated to the data from the meteorological station. The wind regimes showed attached flow acceleration over the airfoil surface for various angles of attack. The results provide a reference to the research and development of vertical axis wind turbine for target markets.

Keywords: Wind sensors, Data logging, correlation, CFD, Airfoil

I. INTRODUCTION

Wind energy is the world major investment target and source of energy for most countries. In recent years, growing climate change concerns and unstable fossil fuel prices have increased the focus on sustainable energy resources, such as wind and solar energy. According to the 2013 Wind Energy data, the worldwide wind capacity reached 296,255 MW by the end of June 2013, out of which 13,980 MW were added in the first six months of 2013. This increase is significantly less than in the first half of 2012 and 2011, when 16,500 MW and 18,400 MW were added, respectively. All wind turbines installed worldwide by mid-2013 can only generate around 3.5% of the world's electricity demand [1], [2].

However, effective use of wind energy requires precise wind resource assessment. Precise wind speed measurements play an important role for estimating the power potential of a wind plant. Generally, according to Zhang et al. [3], wind resource assessment includes:

- (a) Onsite wind conditions measurement
- (b) Correlations between onsite meteorological towers to fill in missing data
- (c) Correlations between long-term weather stations and short-term onsite meteorological towers
- (d) Analysis of the wind shear and its variations

- (e) Modeling of the distribution of wind conditions
- (f) Prediction of the available energy at the site

The common wind assessment Measure-Correlate-Predict (MCP) techniques include: Linear regression model, Variance ratio, Weibull scale, Artificial Neural Networks (ANNs), Support Vector Regression (SVR), Mortimer and wind index MCP [4]. These methods make use of historical wind data series which are available for nearby climatological weather stations used as reference stations [5]. The wind data of the reference station must coincide in length and date with a measuring period for the candidate site.

Most of MCP methods have made use of linear regression algorithms to establish the relationship between hourly intervals of time wind characteristics of the candidate site and of the weather station chosen as the reference site [5], [6], [7]. In addition, a number of models have also been proposed to establish non-linear type relationships [8]. However, the linear algorithms are easy to compute and hence easy interpretation.

Wind power can be made economically feasible through maximum conversion of wind turbine efficiency from wind energy to mechanical energy. Wind turbines are classified into horizontal-axis wind turbine (HAWT) and vertical-axis wind turbine (VAWT). Compared to the horizontal axis wind turbines, the vertical-axis wind turbines can be effectively used in urban areas where wind has characteristics of unsteadiness with turbulence. The VAWT can be broadly divided into three basic types: Savonius type, Darrieus type, and Giromill type [5]. In the small-scale wind turbine market, the simple straight-bladed Darrieus VAWT is more attractive for its simple blade design. This configuration can be classified as fixed and variable pitch VAWTs, and it has been found out that the fixed pitch provides inadequate torque [6]. Most of the previous research activities on Darrieus type VAWT equipped with National Advisory Committee for Aeronautics (NACA) 4-digit (XX00) series symmetric airfoils (NACA0012, NACA0015 and NACA0018) were unable to self-start. Among different aspects involved for the inability to self-start is due to several factors (like technical aspects, inadequate research work and funding), and the most dominant ones are due to aerodynamic factors which are key determinant for maximum wind turbine efficiency [9], [10], [11], [12].

In this study, the linear regression metric model is used to correlate wind data measurements obtained by meteorological station and reference optical sensor anemometers. Based on

wind regime of specific locations, an analysis of aerodynamic performance and flow field structure of two-dimensional simulations on NACA0015 airfoil was done using CFD FLU-ENT software. The towns of Garissa ($0^{\circ}28'S, 39^{\circ}38'E$) and Marsabit ($2^{\circ}19'N, 37^{\circ}58'E$), both rural-urban towns in North-Eastern Kenya, have been selected as potential sites for the study. Since most wind turbines site evaluations are designed for hubs above 50 m, the study calculations will provide a new reference for the development of the small vertical axis wind turbines at heights below 50 m. This will reduce increased hub height cost arising from construction of support towers.

II. MATERIALS AND METHODS

A. Optical encoders

An optical encoder transducer was used to generate coded reading of a measurement. Shaft encoders were used for measuring angular displacement and velocity. The anemometer and wind vane sensors in this study were developed using the incremental and absolute encoders, respectively, to generate digital signals. Advantages of digital transducers over analog ones include high resolution, high accuracy and relative ease of adaptation in digital control systems.

B. Measure-Correlate-Predict (MCP) metrics

In this study, the linear regression and variance ratio component MCP methods are utilized due to their simplicity [3]. Linear regression method applies a power law relationship between the reference and the site wind speed to provide a better long-term prediction of the wind resource at the site. It is a common method used to characterize the relationship between the reference and target site wind speeds. The prediction equation is expressed as:

$$f(x) = mx + b \quad (1)$$

where $f(x)$ is the predicted wind speed at the target site; x is the observed wind speed at the reference site; and m and b are the estimated intercept and slope of the linear relationship, respectively.

The values of the slope m and y-intercept b are deduced when forcing the mean and variance of the wind speeds estimated during the period of concurrence (short-term) of data between the target and reference sites to coincide with the mean and variance of the wind speeds observed over that period [3], [5]. Therefore, Equation (1) is transformed into:

$$f(x) = \mu_y - \frac{\sigma_y}{\sigma_x} \mu_x + \frac{\sigma_y}{\sigma_x} x \quad (2)$$

where μ_x , μ_y , σ_x and σ_y are the mean averages and standard deviation for the experimental and reference data respectively. Since the aim of the study was to assess the wind resource of the meteorological measurements in comparison to the measurements by the developed optical instruments for a target site, the choice and application of other metric methods is beyond the scope of this study.

The relationship between the two sets of data is further expressed mathematically in terms of a correlation coefficient,

which is commonly referred to as a correlation. The correlation is a measure of how closely the two variables move and always take on a value between 1 and -1 [13]. It is expressed as:

$$r(x, y) = \frac{Cov(x, y)}{\sigma_x \sigma_y} \quad (3)$$

where, $r(x, y)$ is correlation of the variables x and y , $Cov(x, y)$ is covariance of the variables x and y , whereas σ_x and σ_y are sample standard deviations of the random variable x and y , respectively.

The covariance is a measure of how two variables are related; normally expressed as:

$$Cov(x, y) = \sum_{i=1}^n \frac{(x_i - \bar{x})(y_i - \bar{y})}{n - 1} \quad (4)$$

where n is the number of days in the sample and \bar{x} and \bar{y} are the mean predicted wind speeds at the experimental target site and reference site, respectively.

C. The power law

The wind profile power law is a relationship between the wind speeds at one height, and those at another. It is often used in wind power assessments where wind speeds at the height of a turbine must be estimated from near surface wind observations, or where wind speed data at various heights must be adjusted to a standard height prior to use. The wind power law was used to convert the wind speed given by meteorological station at height of 10 m to the experimental heights [14]. The power law is expressed as:

$$\frac{v_2}{v_1} = \left(\frac{h_2}{h_1} \right)^\alpha \quad (5)$$

where v_2 and v_1 are the mean wind speed at heights h_2 and h_1 , respectively. The exponent α is an empirically derived coefficient that depends on such factors as surface roughness and atmospheric stability. Numerically it lies in the range 0.05-0.5, with the most frequently adopted value being 0.14 (widely adopted to low surface and well-exposed sites) as a good representative of the prevailing conditions. For instance, for Marsabit meteorological conditions, α is approximately 0.16 [15].

D. Experimental techniques

1) *Study design:* In Fig. 1, the overall schematic block diagram to measure wind speed and wind direction is shown. A rotational anemometer and a wind vane with optical sensors are used to measure the wind speed and direction, respectively. The output signals of these instruments are fed into a Microcontroller-based data logger. The optical sensor in the anemometer is used to generate a certain number of pulses in units of time depending on the rotational speed of the shaft. The Microcontroller-based data logger is then used to determine the wind speed by counting the number of pulses. The output from the data logger is displayed on a 162 LCD display; which is a small low cost display. It is easy to interface

it with a microcontroller because it has an embedded controller which is standard across many microcontrollers [16].

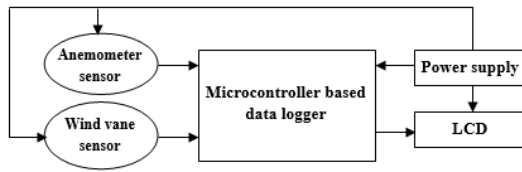


Fig. 1. Block diagram of the overall scheme

2) *Measuring of wind speed and direction:* The wind sensors were clamped on a horizontal metallic support masked on a strong metallic vertical stand above the surface. The wind sensors were separated well enough to avoid the flow disturbance due to the blowing wind. The signals from both anemometer and wind vane sensors were fed to CR 10 Campbell microcontroller-based data logger which was used to measure 4 seconds averaged wind data, which it further averaged for one hour and stored in the EEPROM for 24 hours. Reading of wind speed was done at interval of 3 times a day alongside conventional instruments at the meteorological station for comparison. Using the power law formula in Equation (1), the meteorological wind speed at standard height of 10 m is converted to the experimental heights. The linear regression method was used to test and establish the correlation between the two measuring systems using the linear regression prediction Equation (2). In addition, Equation (3) was used to ascertain the closeness of predicted wind speed to the measured mean.

According to [17], symmetric (NACA0015) airfoils are utilized to have the same characteristics of lift and drag on upper and lower surfaces; they provide lift during complete 360 rotation of the vertical axis wind turbine. That implies there will be no need to readjust the blades in the direction of wind because the blade will provide lift irrespective of wind direction. Therefore, the major wind parameter in this study is the wind speed as opposed to wind direction.

3) *Software design:* The language used is C which is a general-purpose programming language that can work on any Automatic Voltage Regulator (AVR) microcontrollers. The AVR studio is used to edit, debug, compile and load the code to the microcontroller's flash memory via STK500 circuit board. The STK500 is a starter kit and a development system used to program Atmel AVR flash microcontrollers. It gives designers a quick start to developing code on the AVR, combined with features for developing prototypes and testing new designs. The STK500 interfaces AVR studio for code writing and debugging. It includes AVR studio software interface, RS-232 interface to PC for programming and configuration and a serial In-System Programming (ISP) of AVR devices. The data logging system flow chart is as shown in Fig. 2.

4) *Principle of operation:* The process begins by switching the power switch and immediately the microcontroller is able to initialize itself and a string is displayed at the LCD screen to indicate successful engagement of the whole system. Signals

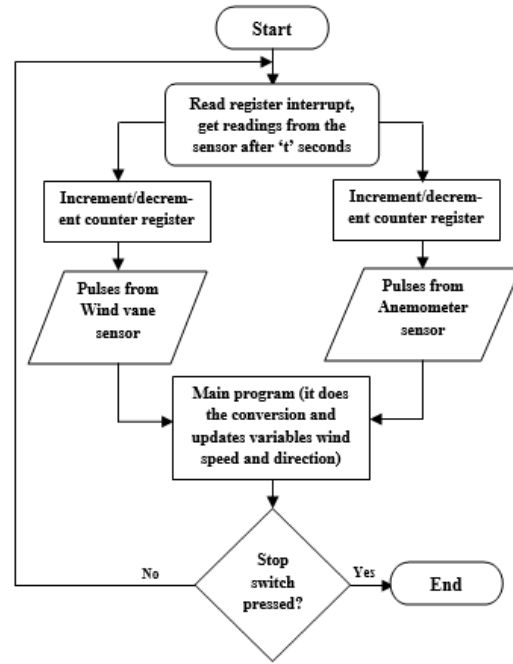


Fig. 2. Data logging system flow chart

generated as a result of measurement of a physical value by the incremental and absolute encoders are directly interfaced to the microcontroller. The program in the microcontroller uses this digital value along with other inputs and preloaded values called calibrations to determine the wind speed and direction, and eventually transmit the measured parameters to the LCD for observation via microcontroller digital interface. Three switches are integrated into the system to provide functionalities which includes start switch for starting the measurement, stop switch for terminating the whole operation and reset switch for resetting the register values thus resetting the values of the measured parameters. The circuit also includes the RS-232 interface connector, serial in-system programming (ISP) connector and linear voltage regulator. The RS-232 Interface is used for interfacing the microcontroller with the PC for data transmission. This is done by connecting a data logger's input/output (I/O) port with a PC's RS-232 port. This interface converts the computer's RS-232 voltage levels to the Complementary Metal-Oxide-Semiconductor (CMOS) levels of the data logger. It also isolates the computer's electrical system from the data logger, thereby protecting against ground loop, normal static discharge, and noise. The ISP connector allows the microcontroller to be programmed and configured by the AVR programmer. The Linear voltage regulator provides DC output voltage and contains circuitry that continuously holds the output voltage at the design value regardless of changes in load current or input. This is due to the fact that every electronic circuit is designed to operate off of some supply voltage, which is usually assumed to be constant. The LM7805 (Appendix A1) is used to provide a constant 5V to power the whole circuit as shown in the

schematic data logging system electronic circuit of Appendix A2.

E. Governing equations and numerical solution

In CFD software, wind turbine airfoils are simulated under the turbulent flow model [18] using Reynolds-averaged Navier-Stokes (RANS) equation defined as:

$$\rho \frac{dU_i}{dt} = \frac{\partial P}{\partial x_i} + \frac{\partial}{\partial x_i} \left[\mu \left(\frac{\partial U_i}{\partial x_j} + \frac{\partial U_j}{\partial x_i} \right) - \rho \overline{U'_i U'_j} \right] \quad (6)$$

where $\rho \overline{U'_i U'_j}$ is the unknown term called Reynolds stresses. The left hand side of the equation describes the change in mean momentum of fluid element and the right hand side of the equation is the assumption of mean body force and divergence stress.

A static NACA0015 airfoil study was conducted to test turbulence models to obtain the suitable model for the airfoil flow field structure investigation. The three turbulent models tested include the two-equation fully turbulent $k-\omega$ shear-stress transport (SST) model, five-equation fully turbulent Reynolds stress model and one-equation fully turbulence Spalart-Allmaras model. This was achieved by comparing the coefficients of lift of the various turbulence models tested with the experimental data by [19]. The 2D domain geometry was created by pointwise, a pre-processor software for generating CFD meshes. The 2D simulated NACA0015 airfoil was meshed with a fully structured C-type grid with 800 nodes over the surface as shown in Fig. 3.

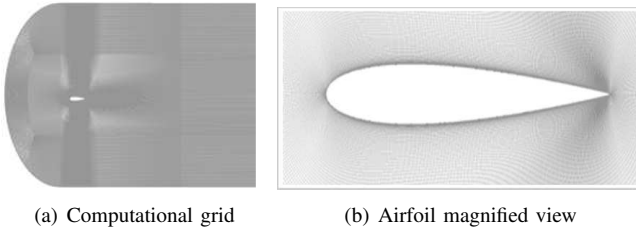


Fig. 3. Computational and Airfoil magnified view grids

Reynolds number for the simulations was $Re = 1.35 \times 10^5$, similar to the reliable wind tunnel test in order to validate the present simulation. Here Reynolds number is defined in terms of the free-stream velocity U_{ref} and the airfoil chord C . The free stream temperature was 300 K, which is the same as the environmental temperature. The turbulence intensity of 0.8% was set and a pressure based unsteady second order was selected. A segregated, implicit solver utilized was ANSYS CFD Fluent 14.5 ©. The total number of cells adopted was 454,404 cells with 800 points distributed on the airfoil surface totally.

F. Airfoil selection

Any rotational forces such as wake rotation, turbulence caused by drag or vortex shedding (tip losses) will further reduce the maximum wind turbine efficiency. The lift and drag coefficients of NACA0012, NACA0015 and NACA0018 series

symmetric airfoils were compared by [10] for vertical axis wind turbines design considerations. It was observed that a low value of lift coefficient and high value of drag coefficient was obtained for NACA0018, while, NACA0012 had a high value of lift coefficient and low value of drag coefficient making it most suitable from aerodynamic characteristics. However, from a systematic numerical study of various airfoils including NACA 4-digit series by [10], [11] based on the Reynolds-Averaged Navier-Stokes (RANS) solutions of the VAWT flows, the authors indicated that thicker sections performed better under low wind speeds. Therefore, for the purposes of our simulations, NACA0015 airfoil profile is chosen for the analysis.

G. Numerical verification

The 2D simulations for various angles of attack were conducted for the whole range of angles of attack from -5° to 15° because it is the operating range of the wind turbine designs [17]. To find the most appropriate turbulence model for this study, different model were selected for testing namely: the two-equation shear stress transport (SST) $k-\omega$ model, one-equation Spalart-Almaras (S-A), and five-equation Reynolds stress models. At low angle of attack, the dimensionless lift coefficient increased linearly with angle of attack and all the tested turbulent models accurately predicted the experimental results until stall. The Spalart-Almaras and Reynolds stress models over predicted the results beyond 13° . The over prediction of drag was expected since when using turbulent models, the flow is assumed to be turbulent everywhere, and does not provide a transition from laminar to turbulent flow. The assumption has the potential of causing some error between the computational and experimental data [17]. Additionally, the Spalart-Almaras turbulence model is applied better in flows with high pressure gradients which this study is far below, considering the low blade chord's Reynolds number.

However, the two-equation $k-\omega$ SST turbulence model gave closer prediction of lift coefficient both in pre-stall and post-stall region than the rest of the turbulence models hence it is considered the best model. The CFD $k-\omega$ SST model is therefore chosen for analyzing NACA0015 airfoil flow field structure based on the site's appropriate blade Reynolds number.

III. RESULTS AND DISCUSSION

A. Wind speed correlation

A linear regression chart was used to test and establish a correlation between wind data from the developed system and meteorological station based on target site wind regimes. The Simple linear regression chart for daily mean wind speed averages were plotted and corresponding correlation obtained as shown in Fig. 4.

From regression chart, and applying Equations (3) and (4), the two sets of measurements had a strong positive correlation of 0.98; showing effectiveness and reliability of meteorological wind instruments.

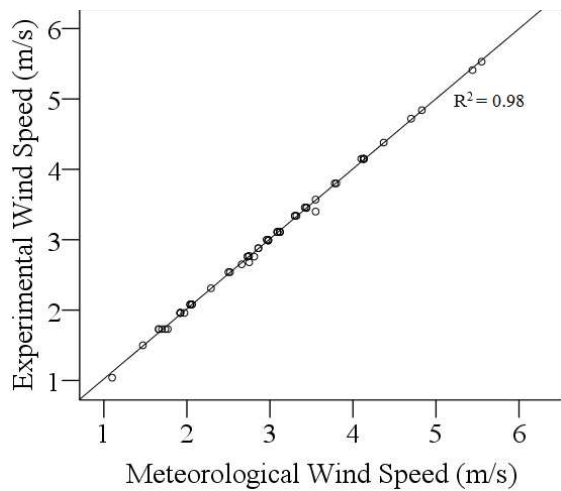


Fig. 4. Linear regression

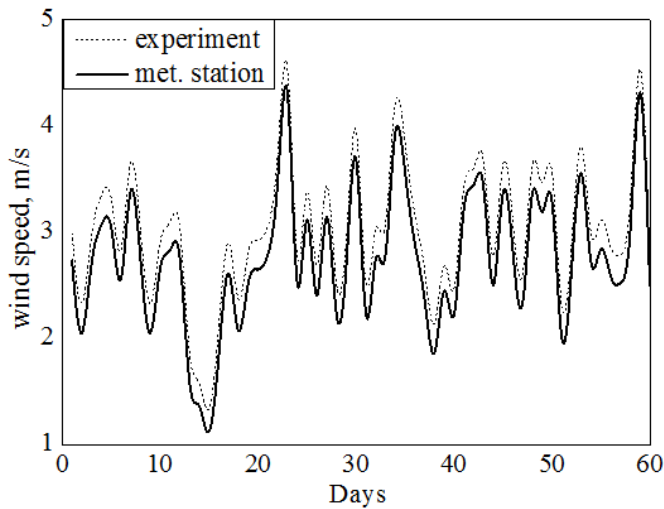


Fig. 5. Wind assessment

The optical anemometer sensor can be used at the site's passages and the wind speed in the free field can be approximated with the data from the meteorological station at various hub heights using the wind power Equation (5). The strong correlation confirms that the experimental anemometer is giving the correct readings and practical readings can be approximated to the data from the meteorological station.

B. Wind speed output

Fig. 5 shows daily mean wind speed output graph for experimental and meteorological measurements collected for a period of two months.

The two sets of wind speed measurements are consistent with another. However, the Meteorological speeds are generated at slightly lower speed as compared with the experimental measurements. This is as a result of minimal mechanical friction offered by the developed optical anemometer sensor as opposed to the conventional mechanical systems at the meteorological station. The meteorological station anemometer has

its shaft directly coupled to an electric generator that generates a.c voltage whose magnitude is directly proportional to the shaft's frequency of rotation. A precision rectifier and a filter are used to convert the a.c voltage generated to d.c voltage that is then directly displayed on a voltmeter calibrated to wind speed. The generated a.c voltage depends on the moving coil and needs to be calibrated frequently, hence, its performance is not very stable and reliable for large variation of wind speed. Therefore, the more mechanical friction experienced associated with mechanical properties by this type of anemometer could be attributed to its many contacting parts. However, the optical anemometer with optical sensors has minimal physical contact with the shaft; hence reduced friction and improved speed limit as they can respond to a shaft rotating at any practically possible speed. The microcontroller-based system receives electronic signals from the sensors as a result of rotation. As the encoder disk rotates, pulses of light from emitter strike a sensor every time a slot on the disk is aligned between them. Each pulse is converted to an electronic pulse by the signal conditioner as opposed to moving coil in the conventional mechanical system from the meteorological station. Therefore in general, the meteorological speed measurements are slightly lower than the experimental wind speed as shown in the Fig. in 5.

C. Flow field structure

Applying $k-\omega$ SST model, simulations for the pressure distribution and flow field structure on NACA0015 airfoil at wind speed of 11 m/s were carried out at various angles of attack. This is the average wind speed recorded at a standard Anemometer height of 10 m at Marsabit station [15]. The simulation results were analyzed in various stages by the CFD-post features in ANSYS. The structure of flow field of NACA0015 under different angle of attack was calculated using $k-\omega$ SST model as shown in Fig. 6.

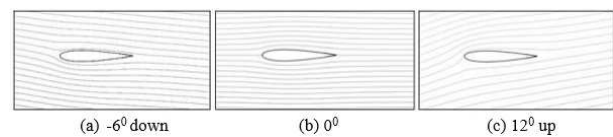


Fig. 6. Flow streamlines of NACA0015 airfoil at 11 m/s

From Fig. 6, the streamlines at angle of attacks -6° , 0° , and 12° show full attached flow, hence, no flow separation at various angles of attack at this wind regimes. This is due to the site's mean speed corresponding to the relatively very small chord Reynolds number. Therefore, the profile is recommended for the vertical wind turbine airfoils operating at the 11 m/s.

D. Pressure coefficients

Fig. 7 shows the variation of pressure coefficient plots and contours for the flow regimes along the Airfoil at different position.

Pressure coefficient plots shows that there is a high pressure at the leading edge (stagnation point) and low at trailing edge.

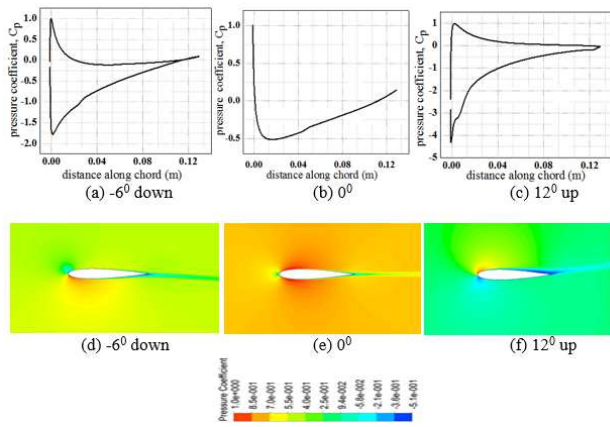


Fig. 7. Pressure coefficient plots and contours

Observe in Fig. 7 that, the variation of pressure distribution on the airfoil surface is high under different angle of attack. The larger the angle of attack, the greater the difference of pressure between the upper and lower surface. The pressure distribution on the airfoil lower surface showed positive values which produce positive lift force when the angle of attack was larger than zero. When the attack angle was zero, the pressure coefficient of airfoil's upper and lower surface was nearly equal to zero. The pressure distribution on the airfoil upper surface showed positive values which produce negative lift force when the angle of attack was larger than zero.

From the pressure coefficients plots and contours, it is observed that the best operating angle of attack for symmetric profiles like NACA0015 is positive. However, for most non-symmetric airfoils, the sliding ratio increases as the wind speed increases at the same operating AOA. Therefore, the non-symmetric airfoils like NREL profiles have a negative best operating AOA with maximum thickness of between 20% and 40% of the chord [17], [20]. Therefore, profiles whose best operating angle of attack (maximum sliding ratio) is positive like NACA00XX series, the maximum thickness occurs at about 50% of chord. Generally all symmetric airfoil belongs to this category.

E. Velocity magnitudes

Fig. 8 shows velocity magnitudes plots for the NACA0015 airfoil profile. On the leading edge, the velocity of flow is nearly equal to zero (stagnation point) but acceleration on the upper surface can be observed from the colour changes of the contour magnitudes. From Figs. 7 and 8, as the fluid

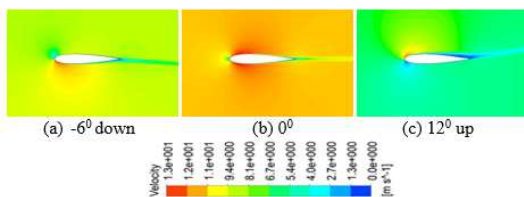


Fig. 8. Velocity magnitude contours

flow accelerates over the airfoil, there is an adverse drop in pressure thus the pressure distribution quickly becomes zero and then reasonably goes to a large a negative value. The pressure then rises as the flow decelerates and the magnitude of the pressure distribution drops. In effect, the wind blade airfoil tends to rotate and the pressure on the lower surface is always higher than the pressure on the upper surface. This agrees with the theoretical Bernoulli's principle; as the velocity of the air increases, pressure coefficient becomes more negative. On the trailing edge, the flow on the upper surface decelerates and merges with the flow from the lower surface.

IV. CONCLUSION

This paper presents wind measurement resource assessment study and a numerical simulation for wind regimes of Marsabit and Garissa, both rural-urban towns in North-Eastern Kenya. Based on these wind regimes, an analysis of aerodynamic performance and flow field structure of 2D numerical simulations on NACA0015 airfoil has been done using CFD FLUENT software. The wind measuring technique of Meteorological measurements was also tested to ascertain its accuracy and effectiveness. The results derived in the study are therefore summarized as follows:

- The Meteorological wind speed measurement correlated with the calibrated cup anemometers sensors with a correlation coefficient of 0.98. This is a strong correlation, therefore, the Meteorological wind data measurement is reliable to predict long-term pattern of wind regime. Also, the strong correlation confirms that the experimental anemometer gives the correct readings and practical readings can be approximated to the data from the meteorological station.
- The fluid flow acceleration over the airfoil at different angles of attack did not cause separation due to relatively low mean wind speed regimes. There was a large velocity gradient on the upper front surface when the angle of attack was relatively large and vice versa. The difference in pressure coefficient between the upper and lower surface is maximum at the point of attack and it is directly proportional to the angle of attack. Therefore, the lift force of an airfoil mainly comes from the front edge.

These calculation results provide a reference to the research and development of vertical axis wind turbine at hub heights below 50 m. This is deemed to reduce increased hub height cost arising from construction of support towers by wind energy industries.

ACKNOWLEDGEMENT

This research work was supported in part by the Institute of Dynamics and Control of Spacecrafts, of School of Astronautics, through Harbin Institute of Technology; and the Chinese Scholarship Council, through P.R. China Government in collaboration with the Kenyan Government.

REFERENCES

- [1] World wind energy association, half year report, June, 2013.
- [2] J. C. Oliveira A. Reis, L. N. Velasco. Computational assessment of control strategy for pmsg wind turbines aiming at voltage regulation on connection point. In *International Conference on Renewable Energies and Power Quality*, volume 13, March 2013.
- [3] Jie Zhang, Souma Chowdhury, Achille Messac, and Bri-Mathias Hodge. Assessing long-term wind conditions by combining different measure-correlate-predict algorithms. In *ASME International Design Engineering Technical Conferences, Portland, Oregon*, volume 3A, August 4th-7th 2013.
- [4] Alejandro Romo Perea, Javier Amezcua, and Oliver Probst. Validation of three new measure-correlate-predict models for the long-term prospection of the wind resource. *Journal of renewable and sustainable energy*, 3(2), 2011.
- [5] Sergio Velázquez, José A Carta, and JM Matías. Comparison between anns and linear mcp algorithms in the long-term estimation of the cost per kwh produced by a wind turbine at a candidate site: A case study in the canary islands. *Applied Energy*, 88(11):3869–3881, 2011.
- [6] Anthony L Rogers, John W Rogers, and James F Maxwell. Comparison of the performance of four measure-correlate-predict algorithms. *Journal of Wind Engineering and Industrial Aerodynamics*, 93(3):243–264, 2005.
- [7] E Sreevalsan, Siddarth Shankar Das, R Sasikumar, and MP Ramesh. Wind farm site assessment using measure-correlate-predict (mcp) analysis. *Wind Engineering*, 31(2):111–116, March 2007.
- [8] Ramón García-Rojo. Algorithm for the estimation of the long-term wind climate at a meteorological mast using a joint probabilistic approach. *Wind Engineering*, 28(2):213–223, March 2004.
- [9] Alexander M Gorlov and Valentin Silantsev. Limits of the turbine efficiency for free fluid flow. *Journal of Energy Resources Technology*, 123:311–317, August 2001.
- [10] M Saqib Hameed and S Kamran Afaq. Design and analysis of a straight bladed vertical axis wind turbine blade using analytical and numerical techniques. *Ocean Engineering*, 57:248–255, January 2013.
- [11] JV Healy. The influence of blade thickness on the output of vertical axis wind turbines. 2:1–9, 1978.
- [12] Mazharul Islam, Amir Fartaj, and Rupp Carriveau. Analysis of the design parameters related to a fixed-pitch straight-bladed vertical axis wind turbine. *Wind Engineering*, 32(5):491–507, October 2008.
- [13] José A Carta and Sergio Velázquez. A new probabilistic method to estimate the long-term wind speed characteristics at a potential wind energy conversion site. *Energy*, 36(5):2671–2685, 2011.
- [14] Lin Lu, Hongxing Yang, and John Burnett. Investigation on wind power potential on hong kong islands an analysis of wind power and wind turbine characteristics. 27(1):1–12, 2002.
- [15] JN Kamau, R Kinyua, and JK Gathua. 6 years of wind data for marsabit, kenya average over 14m/s at 100m hub height; an analysis of the wind energy potential. *Renewable Energy*, 35(6):1298–1302, June 2010.
- [16] Douglas Lewin and David Noaks. *Theory and design of digital computer systems*. Nelson, 1980.
- [17] Mohamed A Sayed, Hamdy A Kandil, and Ahmed Shaltot. Aerodynamic analysis of different wind-turbine-blade profiles using finite-volume method. *Energy Conversion and Management*, 64:541–550, December 2012.
- [18] Ahmed M El Baz, Aly R Refaey, Mohannad Y Mohammed, and Abdallah W Youssef. Computational modelling of h-type darrieus-types vertical axis wind turbine with multi element airfoil blades. *Eleventh International Conference of Fluid Dynamics*, 11(ICFD11-EG-4039), December 19-21 2013.
- [19] Robert E Sheldahl and Paul C Klimas. Aerodynamic characteristics of seven symmetrical airfoil sections through 180-degree angle of attack for use in aerodynamic analysis of vertical axis wind turbines. Technical report, Sandia National Laboratories, March 1981.
- [20] Mazharul Islam, David S-K Ting, and Amir Fartaj. Aerodynamic models for darrieus-type straight-bladed vertical axis wind turbines. *Renewable and Sustainable Energy Reviews*, 12(4):1087–1109, 2008.

V. APPENDICES:

A. Appendix A1: ATmega32 Pin Descriptions

The following is a summary of Atmel ATmega32 micro-controller Pin descriptions

VCC Digital supply voltage.

LM7805 Constant 5V circuit supply source.

GND Ground.

Port A (PA7..PA0) Port A serves as the analog inputs to the A/D Converter. Port A also serves as an 8-bit bi-directional I/O port, if the A/D Converter is not used. Port pins can provide internal pull-up resistors (selected for each bit). The Port A output buffers have symmetrical drive characteristics with both high sink and source capability. When pins PA0 to PA7 are used as inputs and are externally pulled low, they will source current if the internal pull-up resistors are activated. The Port A pins are tri-stated when a reset condition becomes active, even if the clock is not running.

Port B (PB7..PB0) Port B is an 8-bit bi-directional I/O port with internal pull-up resistors (selected for each bit). The Port B output buffers have symmetrical drive characteristics with both high sink and source capability. As inputs, Port B pins that are externally pulled low will source current if the pull-up resistors are activated. The Port B pins are tri-stated when a reset condition becomes active, even if the clock is not running. Port B also serves the functions of various special features of the ATmega32.

Port C (PC7..PC0) Port C is an 8-bit bi-directional I/O port with internal pull-up resistors (selected for each bit). The Port C output buffers have symmetrical drive characteristics with both high sink and source capability.

As inputs, Port C pins that are externally pulled low will source current if the pull-up resistors are activated. The Port C pins are tri-stated when a reset condition becomes active, even if the clock is not running. If the JTAG interface is enabled, the pull-up resistors on pins PC5(TDI), PC3(TMS) and PC2(TCK) will be activated even if a reset occurs. The TD0 pin is tri-stated unless TAP states that shift out data are entered. Port C also serves the functions of the JTAG interface and other special features of the ATmega32.

Port D (PD7..PD0) Port D is an 8-bit bi-directional I/O port with internal pull-up resistors (selected for each bit). The Port D output buffers have symmetrical drive characteristics with both high sink and source capability. As inputs, Port D pins that are externally pulled low will source current if the pull-up resistors are activated. The Port D pins are tri-stated when a reset condition becomes active, even if the clock is not running. Port D also serves the functions of various special features of the ATmega32.

RESET Reset Input. A low level on this pin for longer than the minimum pulse length will generate a reset, even if the clock is not running. Shorter pulses are not guaranteed to generate a reset.

XTAL1 Input to the inverting Oscillator amplifier and input to the internal clock operating circuit.

XTAL2 Output from the inverting Oscillator amplifier.

AVCC The supply voltage pin for Port A and the A/D Converter. It should be externally connected to VCC, even if the ADC is not used. If the ADC is used, it should be connected to VCC through a low-pass filter.

AREF The analog reference pin for the A/D Converter.

B. Appendix A2: Microcontroller-based Data Logger Schematic Circuit

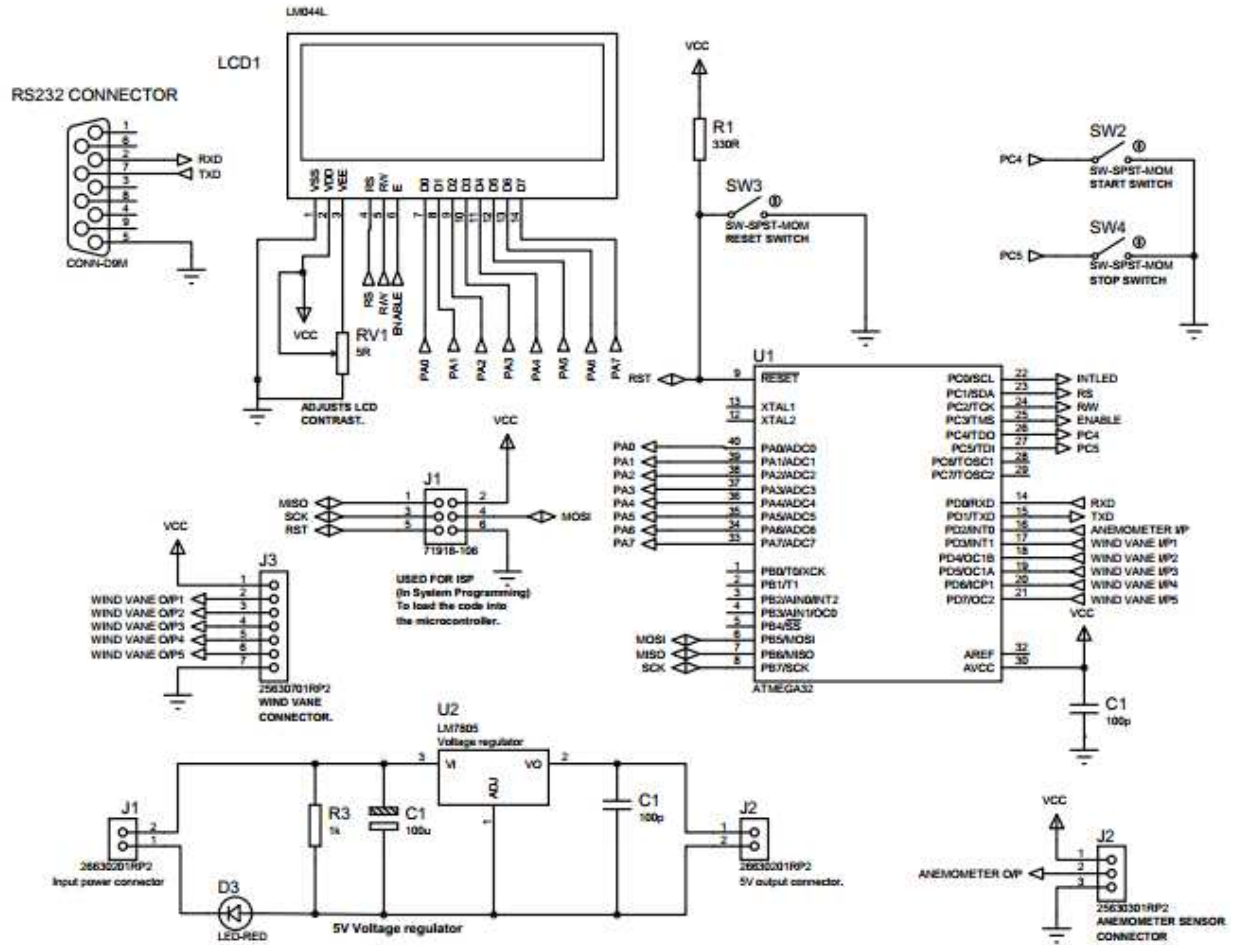


Fig. 9. Appendix A2: Microcontroller Based Data Logger Schematic Circuit